Are eruptions from linear fissures and caldera ring dykes more likely to produce pyroclastic flows?

D.E. Jessop, J. Gilchrist, A.M. Jellinek, Olivier Roche

Are eruptions from linear fissures and caldera ring dikes more likely to produce pyroclastic flows?

D. E. Jessop[a,b,*], J. Gilchrist[b], A. M. Jellinek[b], O. Roche[a]

[a] *Laboratoire Magmas et Volcans, Universeé Blaise Pascal-CNRS-IRD, OPGC, Clermont-Ferrand, France*
[b] *Department of Earth, Ocean and Atmospheric Sciences, University of British Columbia, Vancouver, Canada*

Abstract

Turbulent volcanic jets are produced by highly-energetic explosive eruptions and may form buoyant plumes that rise many tens of kilometres into the atmosphere to form umbrella clouds or collapse to generate ground-hugging pyroclastic flows. Key to which of these two behaviours will occur is the extent to which the mechanical entrainment and mixing of ambient air into the jet by large (entraining) eddies forming the jet edge changes the density of the air-ash mixture: low entrainment rates lead to pyroclastic flows and high entrainment rates give rise to buoyant plumes. Recent experiments on particle-laden (multi-phase) volcanic jets from flared and straight-sided circular openings suggest that the likelihood for buoyant plumes will depend strongly on the shape and internal geometry of the vent region. This newly recognised sensitivity of the fate of volcanic jets to the structure of the vent is a consequence of a complex dynamic coupling between the jet and entrained solid particles. Building on this work, here we use an extensive series of experiments on multi-phase turbulent jets from analogue linear fissures and annular ring fractures to explore whether the restrictive vent geometry during cataclysmic caldera-forming (CCF) eruptions will ultimately lead a relatively greater frequency of pyroclastic flows than eruptions from circular vents on stratovolcanoes. Our results, understood through scaling analyses and a one-dimensional theoretical model, show that entrainment is enhanced where particle motions contribute angular momentum to entraining eddies. However, because the size of the entraining eddies scales approximately with vent width, the extent of entrainment is reduced as the vent width becomes small in comparison to its length. Consequently, our work shows that for specified mass eruption rates, the high length-to-width ratio vents typical of CCF events are more likely to produce pyroclastic flows. We suggest that the enigmatic proclivity in the geological record for the largest CCF eruptions to produce pyroclastic flows is an expected consequence of their being

*Corresponding author
Email address: d.jessop@opgc.fr (D. E. Jessop)

erupted through continuous or piece-wise continuous caldera ring fractures.

Keywords:

Turbulent Entrainment; Volcanic Jets; Pyroclastic Flows; Caldera Formation; Column Collapse

1. Introduction

Volcanic jets are turbulent, particle-laden (multi-phase) flows that may rise as a buoyant plume high into the atmosphere, forming an umbrella cloud, or undergo catastrophic gravitational collapse to produce devastating pyroclastic flows (PFs). Which of these behaviours occurs depends on the source conditions governing the strength and shape of the jet (e.g. Wilson et al., 1980, and references therein), the stratification (i.e. density profile) of the atmosphere and, more critically, on the extent to which ambient air is entrained into the jet (e.g. Woods, 2010). A remarkable feature in the deposits related to the largest catastrophic caldera-forming (CCF) events is that ignimbrites formed by pyroclastic flows are commonly much more voluminous than deposits resulting from ash fall out from sustained buoyant plumes (e.g. Lipman, 1984; Cole et al., 2005; Cas et al., 2011; Ferguson et al., 2013). Furthermore, many caldera-related deposit sequences consist of basal ash-fall layers with upper thick ignimbrites, suggesting a shift in eruptive dynamics (Druitt and Sparks, 1984).

The size of eruptions can be inferred from the volume of their deposits using the magnitude scale (Mason et al., 2004),

$$M = \log_{10}(\rho_b V_t) - 7 \tag{1}$$

where ρ_b is the bulk density and V_t is the total erupted (bulk) volume. For a volume of ignimbrite, V_i, the ratio V_i/V_t generally correlates with M but, as figure 1 shows, the slope suddenly increases beyond a certain "critical" magnitude which we take to be $M_{\text{crit}} \approx 7.5$ and which corresponds roughly to the transition from the "hyperactive" to "super-eruption" regime (Jellinek and DePaolo, 2003; Jellinek, 2014). In the latter, magma is stored gradually over time, rather than being erupted periodically, in very large magma chambers that form large calderas and large deposits when they eventually erupt (Mason et al., 2004). Whether this correlation is a significant indicator of the distinctive dynamics of such caldera-forming eruptions compared to eruptions from circular vents on stratovolcanoes, or simply a consequence of preservational bias is unclear. Super eruptions have $M > 8$ (i.e. $V_t > 400$ km^3) and occur infrequently, roughly every 10^4–10^5 years on the global scale, and eject 10^3–10^4 km^3 of pyroclastic material (Smith, 1960; Mason et al., 2004; Wilson, 2008; Miller and Wark, 2008). A provocative issue is, thus, whether caldera eruption columns are unstable simply because of their large size or whether

their typical eruption column dynamics are being influenced by the linear or annular vents through which material is injected into the atmosphere.

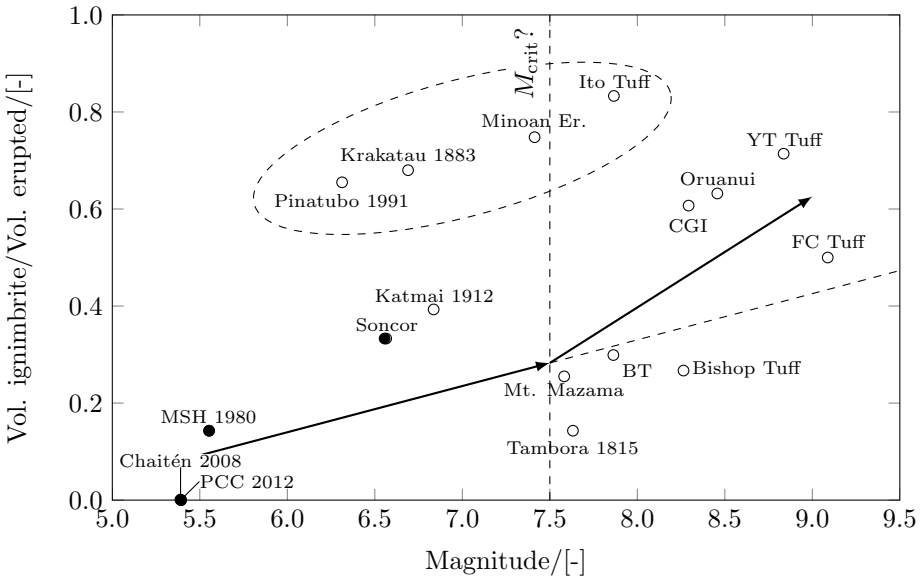

Figure 1: Ratio of ignimbrite volume, V_i, to total magma volume, V_t, produced for 17 historic and pre-historic silicic eruptions as a function of the eruption magnitude, $M = \log_{10}(\text{erupted mass}/[\text{kg}]) - 7$. The arrows give a suggested trend for the ignimbrite/total volume ratio with magnitude. Details of the eruptions are given in §5.3. The caldera-forming eruptions shown are, in order of decreasing magnitude: Fish Canyon Tuff (FC Tuff); Younger Toba Tuff (YT Tuff); Oruanui Ignimbrite; Cerro Galán Ignimbrite (CGI); Bishop Tuff; Ito Tuff; Bandelier Tuff (BT); Tambora 1815; Mount Mazama; Santorini (Minoan eruption); Katmai 1912; Krakatau 1883; Pinatubo 1991; Chaitén 2008. Three non caldera-forming eruptions are shown for reference with filled points: Lascar (Soncor); Mt. St. Helens 1980/05/18 (MSH 1980); Puyhue-Cordón Caulle 2012 (PCC 2012). References for these deposits/eruptions can be found in the supplementary material.

Typically, the rate of turbulent entrainment is characterised by relating the inflow rate of ambient air to the mean rise rate of a turbulent jet through an entrainment coefficient (Morton et al., 1956),

$$\alpha_e \equiv u_{\text{in}}/\bar{u}, \tag{2}$$

where u_{in} is the speed at which ambient air is entrained into the jet and $\bar{u}$ is the mean vertical jet velocity (Morton et al., 1956; Woods, 2010, and figure 2). It is commonly assumed that α_e is a constant with values in the range 0.1 for momentum dominated jets to 0.15 for buoyant plumes (Morton et al., 1956; Fischer et al., 1979), though more recent work has shown that α_e may in fact vary as the buoyancy, velocity and turbulent shear stress profiles evolve with height (Kaminski et al., 2005; Paillat and Kaminski, 2014a).

A mechanical clue to the potential for differing dynamics of entrainment into volcanic jets from circular, linear and annular vents is illustrated in figure 2. We infer from experimental investigations

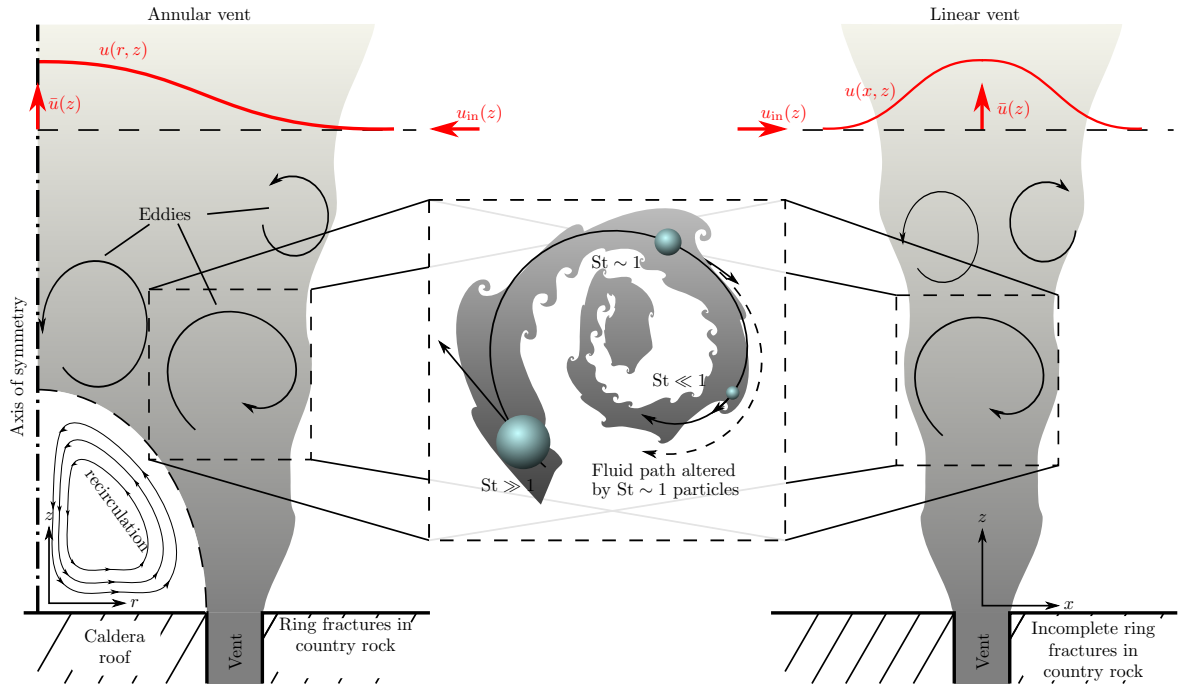

Figure 2: Schematics of the turbulent structure of a volcanic jet from (left) an annular vent and (right) from a linear vent. We show the time-averaged velocity profiles, $u(r,z)$ and $u(x,z)$ (—) and a region of recirculation just above the annular vent. (Inset) particle-eddy coupling regimes according to St. Particles with St $\sim$ 1 can stretch the eddies to which they are coupled.

of incompressible jets from annular vents that, just downstream of the caldera roof, a zone of steady recirculation forms and that the jet remains annular for some distance (e.g. Ko and Chan, 1978; Del Taglia et al., 2004). This annular flow causes the dynamics of the jets with annular vents to differ from jets with circular vents, notably in the strain rates ($\dot{\gamma} \approx \bar{u}/l$) close to the vent which, in turn, affect entrainment into the jet.

Vent geometry affects the dynamics of a multi-phase volcanic jet in two ways: i) the cross-sectional area modulates the mass eruption rate (MER), and eruptions with high MER tend to produce jets that rise high into the atmosphere to form buoyant plumes, whereas low MER eruptions tend to form collapsing fountains (Wilson, 1976); ii) vent shape and internal geometry influences the structure of entraining eddies as well as the trajectories of inertial particles with knock-on effects for the ability of the relatively dense jet to entrain ambient air and become buoyant (Jessop and Jellinek, 2014). The effect of vent geometry has been explored in the context of particle-free, trans-sonic volcanic jets (e.g. Wilson et al., 1980; Koyaguchi et al., 2010; Ogden, 2011). Under these conditions, vent radius, crater structure and pressure at the vent govern the MER.

Entrainment into jets from linear vents without particles has been well studied (e.g. Kotsovinos,

1977; Paillat and Kaminski, 2014b). In experiments on jets from vents that are much longer than they are wide, velocity profiles across the widths of these flows are similar in form to those characteristic of axisymmetric jets (Morton et al., 1956). Consequently, a similar entrainment hypothesis (cf eq. 2) can be applied along with similar conditions for the likelihood that a volcanic jet will rise as a buoyant plume or collapse to form a pyroclastic flows.

Because of the high vent aspect ratio of jets erupted from fissures Glaze et al. (2011) proposed that such eruptions will inevitably involve more extensive entrainment relative to jets from circular sources for specified mass eruption rates. Whether this picture is true and how it is affected by the particulate component of eruptions is unclear. More generally though, most previous works assume implicitly that the major effect of particles is to contribute only to the bulk density of the flow (Veitch and Woods, 2000). Models for jet evolution based on the entrainment hypotheses consequently require either that particles are perfectly coupled (i.e. the particles exactly follow fluid streamlines) and contribute to the mean physical properties of the flow or else that the particles decouple from the flow and sediment quasi-instantaneously from the jet margins and play no further role in driving flow of the jet (e.g. Woods, 1988). A useful metric for particle-fluid stress coupling in a turbulent flow is the Stokes number,

$$\mathrm{St} = \frac{\tau_p}{\tau_e} = \frac{\rho_p d_p^2}{18 f \mu} \frac{u_e}{l_e}, \tag{3}$$

which is a ratio of the response time of a particle τ_p to flow accelerations imparted on an eddy overturn time $\tau_e \sim l_e/u_e$, where u_e is proportional to the mean vertical flow speed. In (3), ρ_p and d_p are the particle density and diameter, respectively, μ is the fluid dynamic viscosity, f is a drag factor of $\mathcal{O}(1)$ (Burgisser et al., 2005). Three different particle-fluid coupling regimes can be defined according the value of St:

$$\mathrm{St} = \begin{cases} \ll 1 & \text{Stokesian - one-way (fluid-particle) coupling} \\ \sim 1 & \text{Inertial - two-way “critical” coupling} \\ \gg 1 & \text{Ballistic - one-way (particle-fluid) coupling} \end{cases}$$

Particle motions are affected by flow accelerations and the structures and momentum fluxes carried by eddies within the flow are, in turn, altered by particle accelerations when $\mathrm{St} \sim 1$ (figure 2, inset, Burgisser et al., 2005, and references therein). In this two-way coupling regime, particles are “critically coupled” to the flow, and we will refer to them as “inertial particles”. By contrast, particles with $\mathrm{St} \ll 1$

are assumed to be perfectly coupled to eddies and particles with $\mathrm{St} \gg 1$ are decoupled from the flow entirely and follow ballistic trajectories. Whereas perfect coupling or sedimentation may be true of the very smallest or largest particles, respectively, volcanic jets contain pumices, ash and lithic clasts of a very wide range of grain sizes, a certain portion of which are critically coupled to the flow and may hence influence the entraining properties of the jet (Crowe et al., 1997; Raju and Meiburg, 1997; Burgisser et al., 2005). To put these regimes into the volcanological context, we have calculated St based on the grain size distribution (GSD) and source/jet conditions in two well-studied eruptions: 1979 Soufrière, St. Vincent (SSV), and 1980 Mount St. Helens (MSH), USA. We note that MSH was about 100 times greater in eruption magnitude than SSV. Details of our calculations are given in the supplementary material. We find that 32% of the GSD has $\mathrm{St} = \mathcal{O}(1)$ for the SSV eruption and 18% for the MSH eruption. Here we infer by $\mathrm{St} = \mathcal{O}(1)$ the portion of the distribution with $0.3 \leq \mathrm{St} \leq 3$. These calculations show that particles with $\mathrm{St} = \mathcal{O}(1)$ represent a significant volumetric fraction of jets generated in explosive volcanic eruptions. In addition to the effects of particle-fluid coupling on entrainment, particle sedimentation from the jet margins can also affect the mean density and internal dynamics of these flows. Particle sedimentation from the jet margins can be quantified through a settling number, $\Sigma_s = v_s(d_p)/\bar{u}$ where $v_s(d_p)$ is the settling velocity of particles of size d_p (Burgisser et al., 2005). Under most natural conditions, however, settling of $\mathrm{St} \sim 1$ particles is a much slower process compared to eddy overturning in the jet and the inertial timescales of these particles. Hence sedimentation has a negligible effect on the dynamics of the jet (Woods and Bursik, 1991; Carazzo and Jellinek, 2012; Jessop and Jellinek, 2014).

In most studies, the explicit and coupled mechanical effects of the three-dimensional geometry of a vent and the presence of inertial particles in the jet on entrainment are neglected. Jessop and Jellinek (2014), henceforth referred to as JJ14, showed that $\mathrm{St} \sim 1$ particles influence entrainment because vent geometry influences the trajectories of inertial particles and these, in turn, stretch the entraining eddies (see inset of Fig. 2). In particular, particles ejected from flared vents contribute angular momentum to and increase the size of entraining eddies, hence enhancing entrainment. Particles ejected from straight-sided vents carry momentum vertically to produce thin, stretched eddies to hence reduce entrainment. As the combination of vent shape and inertial particles affects the mixing of the jet, the structure of the ash cloud and hence the sedimentation regime are affected in turn (Carazzo and Jellinek, 2012). This result predicts substantially different ash-fall deposit architectures produced by jets from straight-sided and flared vents and an evolution in sedimentation regime with vent erosion

during an eruption (Carazzo and Jellinek, 2012, JJ14). This picture is in marked contrast to previously proposed models for the dynamics of volcanic jets that generally assume a point source (e.g. Woods, 1988, 2010).

Although the straight and flared circular vent geometries discussed in JJ14 are typical of eruptions from stratovolcanoes, eruptions from linear fissures and ring dikes related to caldera subsidence, which may in part be structurally controlled, dominate the geological record of caldera-forming eruptions (e.g. Lipman, 1997; Aguirre-Diaz and Labarthe-Hernandez, 2003; Mason et al., 2004; Kennedy et al., 2008; Cole et al., 2010). During caldera-forming events, subsidence of relatively thin, laterally-extensive chamber roofs and along continuous (e.g. Mt. Mazama, Bacon, 1983; Long Valley Caldera, Hildreth and Mahood, 1986; Wilson and Hildreth, 1997) or partly continuous (e.g. Poris formation, Brown and Branney, 2004; Permian Ora Ignimbrite, Willcock et al., 2013; Bad Step Tuff, Branney et al., 1992) ring fractures probably follows initial chamber decompression (Druitt and Sparks, 1984; Roche and Druitt, 2001) and ultimately drives a protracted eruption through a ring dike with geometric properties that vary as the eruption proceeds (e.g. Druitt and Sparks, 1984; Lipman, 1984; Hildreth and Mahood, 1986; Folch and Martí, 2004; Kennedy et al., 2008).

Large-volume and large MER eruptions from purely linear vents (e.g. a dyke extending to the surface) have been inferred purely from field data (e.g. Soldier Meadow Tuff, Korringa, 1973) and from field data along with contemporary observations (Tarawera 1886, Walker et al., 1984) and yet it has not been well understood how a linear vent could retain its shape and hence sustain a high MER, and not evolve to a more stable, circular form with a more restricted MER. Recently, however, Costa et al. (2011) showed that in regions of crustal extension (e.g. Taupo, NZ; Sierra Madre Occidental, Mexico Aguirre-Diaz and Labarthe-Hernandez, 2003; Cole et al., 2010, for example), even moderate extensional stress (40 MPa) is sufficient to sustain the linear vent shape and thus produce very large MER ($\sim 10^{10}$ kg/s) eruptions.

In this paper, we use experiments, theory and field data analysis to test and confirm the hypothesis that the particular mechanics of entrainment into multi-phase volcanic jets erupting from partial (piecewise continuous fissures) or complete (continuous) caldera ring dikes ultimately favour jet instability and, in turn, the production of pyroclastic flows. We will argue that CCF events are generally more likely to produce massive ignimbrites than stratovolcanoes and that the remarkably regular occurrence of these deposits with the largest events is expected. Critically, we will show that this expectation is related to not simply the geometry of volcanic vents but also dynamically related to the coupling of

these jets to the particles they carry into the atmosphere.

2. A simple model for entrainment dynamics

In order to entrain and mix ambient fluid (such as atmospheric air) into a turbulent jet, the eddies at the edge of the jet must do work to penetrate, deform, and overturn the density interface defining the edge of the jet. The work to ultimately irreversibly mix the jet and ambient fluid is extracted from the kinetic energy (KE) carried by the jet. The ratio of KE available to the change in gravitational potential energy in overturning the interface is commonly expressed in terms of a local Richardson number, $\mathrm{Ri} = g'b/\bar{u}^2$ where b and $\bar{u}$ are the local values of jet radius and mean axial velocity, respectively (e.g. Linden, 1973). The reduced gravity is $g' = g(\rho_a - \rho)/\rho_0$ with ρ, ρ_a and ρ_0 the densities of the jet, local ambient fluid and a reference location (typically taken to be the density of the ambient fluid at the level of the vent), respectively, and g the gravitational acceleration. Ri equally expresses the local balance between stabilising buoyancy and destabilising inertial forces (Linden, 1973). However, as a metric for jet strength in our experiments, it is convenient to define Ri in terms of conditions controlled at the source,

$$\mathrm{Ri}_0 = \frac{g'_0 L_0}{\bar{u}_0^2}, \tag{4}$$

where, for all variables, a subscript 0 represents a value at the source, $L_0 = \sqrt{A_0/\pi^s}$ is a length scale for a given nozzle shape defined by the flux through the opening area, A_0 and $s = 0$ for linear vents and $s = 1$ for annular vents. Rectangular (linear) vents are defined by a width, $2l_w$, and breadth, $2l_b$, (Fig. 3b) hence $A_0 = 4l_b^2/\epsilon$ where $L_0 = 2l_b\epsilon^{-1/2}$ and $\epsilon = l_b/l_w$. Annular nozzles are defined by a gap size, d, and overall diameter, d_0 (Fig. 3c) so that $A_0 = \pi d_0^2/4(2\epsilon - \epsilon^2)$ where the nozzle aspect ratio is $\epsilon = d/d_0$. Therefore, $L_0 = d_0/2\sqrt{2\epsilon - \epsilon^2}$. Ri in the jet evolves with height and, generally, we may write $\mathrm{Ri} \propto |\mathrm{Ri}_0|$. A coefficient of proportionality, β, relates $|\mathrm{Ri}_0|$ to Ri so we may therefore write, for an annular vent,

$$\beta = \frac{\mathrm{Ri}}{|\mathrm{Ri}_0|} \propto \left(\frac{\bar{u}_0}{\bar{u}}\right)^2 \frac{1}{\sqrt{2\epsilon - \epsilon^2}}, \tag{5}$$

whereas the definition of L_0 for a rectangular nozzle gives

$$\beta \propto \left(\frac{\bar{u}_0}{\bar{u}}\right)^2 \sqrt{\epsilon}. \tag{6}$$

These two expressions for β indicate the extent to which KE available at the source (i.e. KE $\sim \bar{u}^2$) is extracted for mixing, depending on vent geometry, ϵ. However, following JJ14, to simplify discussion of our results we introduce a more intuitive metric $\lambda = 1/\beta$: when λ is large, more energy is supplied to do the work of overturning the stratification and cause mixing.

Steady jets can be described through coupled equations for the conservation of flux of specific volume, $q = b^2\bar{u}$, momentum, $m = b^2\bar{u}^2$, and buoyancy, $f = g'b^2\bar{u}$. Equivalently, a closed system can also be obtained by replacing f by the conservation of particle mass flux, $p = \phi b^2\bar{u}$, and the effect of dilution on g' (see appendix of Carazzo and Jellinek, 2012). Here, ϕ is the particle volume fraction (i.e. monodisperse GSD) and thus the jet bulk density is $\rho = (1-\phi)\rho_a + \phi\rho_s$ where ρ_s is the particle density. In this case, the effects of environmental stratification are encompassed in the g' parameter. Particle mass flux is a balance between the upward transport of particles by the jet and particle loss through sedimentation, though the latter is comparatively small for the jets considered here. In the "top-hat" formalism (cf. Morton et al., 1956; Woods, 2010) these conservation principles can be expressed as (for axisymmetric jets)

$$\frac{\mathrm{d}q}{\mathrm{d}z} = 2\alpha_e\sqrt{m}, \quad m\frac{\mathrm{d}m}{\mathrm{d}z} = g'q^2, \quad \frac{\mathrm{d}p}{\mathrm{d}z} = 0. \tag{7}$$

It is apparent from these relationships that the jet radius can be expressed as $b = q/m^{1/2}$. The jet angle, θ, is then given by

$$\frac{\mathrm{d}b}{\mathrm{d}z} = 2\alpha_e - \frac{|\mathrm{Ri}_0|}{2\lambda} = \tan\theta. \tag{8}$$

For a linear jet, an equivalent expression can be obtained by writing the two-dimensional conservation equations as per Paillat and Kaminski (2014a) and differentiating to obtain

$$\frac{\mathrm{d}b}{\mathrm{d}z} = \frac{4}{\sqrt{\pi}}\alpha_e - \frac{\sqrt{2}}{\lambda}|\mathrm{Ri}_0| = \tan\theta. \tag{9}$$

The system of equations (7) is sufficient to model the rise and spread of turbulent jets as all the details of how fluid is entrained into the flow are contained within α_e (Morton et al., 1956). We note that, for multi-phase flows, α_e must therefore implicitly describe the influence of the source geometry and inertial particles on entrainment dynamics whereas $\lambda \propto (\bar{u}/\bar{u}_0)^2$ is a measure of how much KE has been extracted from the flow relative to how much was present at the source. We will make experimental measurements of θ as a function of the source conditions and use (8) to infer how α_e and λ vary

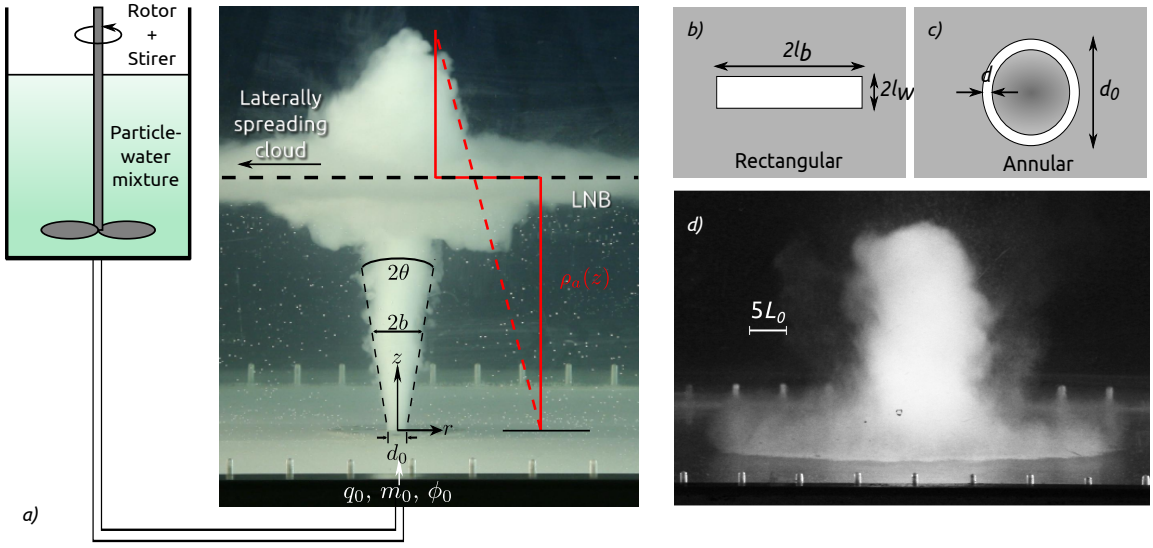

Figure 3: a) Schematic of experimental set up and the measurements taken. Definitions of dimensions for b) rectangular and c) annular vents. An image of a collapsing fountain from an experiment using the linear vent.

according to these conditions.

3. Experiments

We performed isothermal experiments similar to JJ14 where a particle-water mixture was injected into a tank of water to produce a particle-laden jet (Fig. 3a). The injection rate was constant and jets were formed through various straight-sided nozzles which had openings that were either annular or rectangular in cross section (Fig. 3b, c). The resulting turbulent jets had a source Reynolds number, $\mathrm{Re}_0 = \bar{u}_0 D_0/\nu$, of $\mathcal{O}\left(10^3\right)$ or greater (Table 1) indicating fully turbulent conditions in these unbounded flows. Here, ν is the kinematic mixture viscosity and the length scale D_0 is the narrowest nozzle gap (d or l_b). We recorded the morphology of these jets and measured the jet opening angle, 2θ, as a function of ϕ_0, Ri_0 and St_0 as shown in figure 3. We explicitly control these source parameters so as to reproduce conditions inferred for natural eruptions (Carazzo and Jellinek, 2012, JJ14). In particular, we note that the values of ϕ_0 are comparable to natural eruptions as discussed in Appendix A.1 (supplementary material). In some experiments, a density stratification was achieved by adding a lower layer of salty water and carefully filling the rest of the tank with fresh water. This "two-layer" setup has been shown to reproduce the effects of more realistic quasi-linear density gradients if the density difference and layer height are carefully chosen to match the value of the linear gradient

(Carazzo and Jellinek, 2012). Although injected mixtures are always denser than the ambient fluid at the source, entrainment, dilution and particle loss can cause the jets to become buoyant plumes (e.g. Woods, 2010; Carazzo and Jellinek, 2012). Some of our experiments consequently produce buoyant plumes while others lead to collapsing fountains. In other experiments, only fresh water was used to fill the tank (Table 1).

We used particles with a mean diameter of 250 μm and standard deviation of 50 μm, determined by passing the materials through a graded range of sieves. All the particles were made of silica and had a density of 2.5 g/cm^3. The particles were chosen so that, for the largest eddies formed at the source, $\mathrm{St}_0 = \mathcal{O}(0.1 - 1)$. The particle size and typical experimental conditions give $\Sigma_{s0} = \mathcal{O}(0.01 - 0.1)$ (Table 1).

We measured the angle from the vertical of the jet, θ, from a stack of 3–5 images taken from a digital camera each taken at intervals of ~ 1 s and infer the steady-state entrainment from this information via (8). We carefully manufactured our annular vents to ensure that they were as symmetric as possible so no variation in entrainment rate linked to varying gap size around the vent was observed in the experiments. Finally, we noted whether the jet formed in each experiment formed a buoyant plume or a collapsing fountain and these findings are reported in Table 1. Because buoyancy reversals cannot occur in unstratified environments, we only report collapsing fountains for experiments with stratification.

4. Results

We present our results for θ as a function of Ri_0 in figure 4. Figure 4a shows results for the annular nozzles of different ϵ, whereas Fig. 4b shows the same parameter space for a rectangular nozzle with $\epsilon = 0.41$. We show solutions to (8) fitted to the data of JJ14 for narrow and broad/flared vents for particle-free and particle-laden jets. Also, to aid interpretation, we have included "isoentrainment" curves which are solutions to (8) with constant α_e and λ: the vertical differences in the isoentrainment curves represent the different values of α_e (curves are higher for larger α_e) whereas horizontal differences represent different values of λ, so that the "roll-off" is quicker for smaller λ. The source particle concentration, ϕ_0 is indicated by a colour scale.

In general, θ increases with ϵ of annular nozzles. In addition particle-laden jets correspond to larger values of α_e and higher values of λ. Particle-free jets from the $\epsilon = 0.42$ annular vent correspond approximately to iso-entrainment curves with $\alpha_e \approx 0.125$ and $\lambda \approx 1$ (Fig. 4a). Approximately particle-

Table 1: Experimental conditions used in this study. A dash in the St_0 and Σ_{s0} fields indicates that no particles were present for that experiment. When the tank was stratified, we report whether the experiment formed a buoyant plume (BP) or a collapsing fountain (CF).

Expt.	Nozzle Shape	ϵ	ϕ_0	Re_0	St_0	Σ_s	$-\mathrm{Ri}_0$	Class
1	annular	0.09	0.000	10 347	–	–	3.46×10^{-7}	–
2	annular	0.09	0.000	14 225	–	–	8.42×10^{-6}	–
3	annular	0.09	0.000	13 929	–	–	3.50×10^{-4}	–
4	annular	0.09	0.009	18 182	0.92	0.02	4.20×10^{-4}	–
5	annular	0.09	0.009	13 475	0.67	0.03	1.08×10^{-3}	–
6	annular	0.09	0.009	14 014	0.59	0.03	9.19×10^{-3}	–
7	annular	0.09	0.019	12 958	0.56	0.03	1.11×10^{-2}	–
8	annular	0.26	0.000	9 896	–	–	1.16×10^{-5}	–
9	annular	0.26	0.000	9 912	–	–	1.02×10^{-4}	–
10	annular	0.26	0.003	4 378	0.28	0.06	1.27×10^{-5}	BP
11	annular	0.26	0.009	4 409	0.29	0.06	3.34×10^{-4}	BP
12	annular	0.26	0.019	3 832	0.26	0.07	7.10×10^{-4}	CF
13	annular	0.26	0.019	3 268	0.22	0.08	1.59×10^{-2}	CF
14	annular	0.42	0.000	3 387	–	–	6.49×10^{-5}	BP
15	annular	0.42	0.000	6 422	–	–	3.66×10^{-4}	–
16	annular	0.42	0.000	3 617	–	–	2.64×10^{-2}	CF
17	annular	0.42	0.000	3 398	–	–	3.28×10^{-2}	CF
18	annular	0.42	0.009	7 768	0.09	0.12	2.24×10^{-2}	–
19	annular	0.42	0.020	6 260	0.07	0.14	5.40×10^{-3}	–
20	annular	0.42	0.020	7 061	0.08	0.13	5.73×10^{-3}	CF
21	annular	0.42	0.000	4 345	–	–	6.03×10^{-3}	BP
22	linear	0.41	0.000	6 495	–	–	9.53×10^{-5}	–
23	linear	0.41	0.000	6 571	–	–	1.89×10^{-2}	–
24	linear	0.41	0.005	6 373	0.28	0.04	3.23×10^{-5}	BP
25	linear	0.41	0.009	6 524	0.29	0.04	7.77×10^{-4}	BP
26	linear	0.41	0.019	18 435	1.48	0.01	2.33×10^{-4}	CF
27	linear	0.41	0.019	15 970	1.26	0.02	5.80×10^{-4}	CF
28	linear	0.41	0.019	5 061	0.23	0.05	8.56×10^{-3}	CF
29	linear	0.41	0.022	5 800	0.26	0.04	8.16×10^{-5}	BP
30	linear	0.41	0.032	6 002	0.28	0.04	3.53×10^{-5}	BP

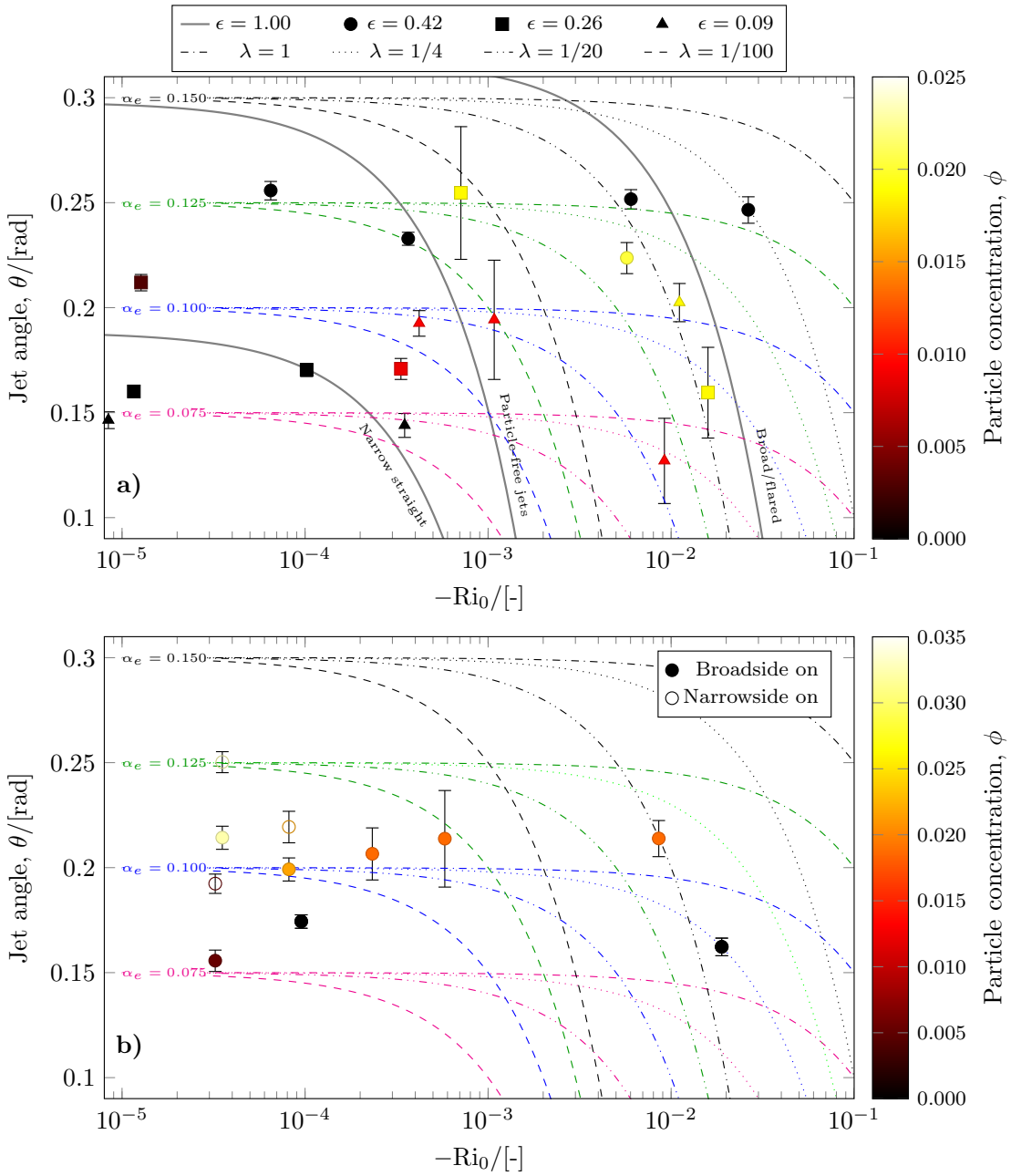

Figure 4: Measured jet angles as a function of $-\mathrm{Ri}_0$ for (a) annular nozzles and (b) a linear nozzle ($\epsilon = 0.41$), where filled and empty symbols represent measurements taken along the broad and narrow sides of the jet. The different shaped symbols in (top) represent different values of ϵ. The colour of the symbol represents the particle concentration, ϕ. We show solutions to (8) (isoentrainment curves) fitted to the data from JJ14 in a) ($\epsilon = 1$) for narrow (straight-sided) nozzles, broad and/or flared nozzles and particle-free jets. We also show solutions to (8) as dotted/dashed curves to aid interpretation of the new data.

Table 2: Values of α_e and λ for the different vent and particle concentrations tested.

Nozzle	ϵ	Condition/ϕ	α_e	λ
8/9	0.42	Particle free/$\phi \approx 0$	0.125	0.25
8/9	0.42	Particle laden	–	–
10	0.26	Particle free/$\phi \lesssim 0.01$	0.100	0.01
10	0.26	Particle laden/$\phi = 0.019$	0.125	0.05
12	0.09	Particle free	0.075	0.01
12	0.09	Particle laden	0.100	0.05
11	0.41	$\phi \lesssim 0.005$	0.075	1
11	0.41	$\phi = 0.019$	0.100	1
11	0.41	$\phi = 0.032$	0.125	1

free jets from the vent with $\epsilon = 0.26$ correspond to $\alpha_e \approx 0.075$, $\lambda \approx 0.01$ whereas higher concentration jets from a vent with the same ϵ have $\alpha_e \approx 0.125$, $\lambda \approx 0.05$. The jet angles formed by jets with $\phi \approx 0$ from the vent with $\epsilon = 0.09$ suggest that $\alpha_e \approx 0.075$ and $\lambda \approx 0.01$ whereas more concentrated jets have $\alpha_e \approx 0.1$ and $\lambda \approx 0.05$. We summarise these results in table 2.

For rectangular vents, a distinctive feature is that the jet angles parallel and perpendicular to the long axes of the vent are not equal (figures 4b, 5a, b), and λ that is almost 5 times larger. Furthermore, we find that θ is systematically smaller parallel to the long axis of the jet than perpendicular to the long axis. However, over a vertical distance of about 10–$15L_0$ the jet width evolves to be approximately equal in both directions, as indicated in figures 5a, b where the widths at $15L_0$ cm are identical. This suggests that the jets from a linear vent with $\epsilon = 0.41$ eventually become axisymmetric, which is further evidenced by the approximately circular deposits (Fig. 5c). We acknowledge, however, that smaller ϵ may produce only elliptical deposits. Particle-laden jets from this linear nozzle ($\phi \approx 0.02$) had $\alpha_e \approx 0.1$ and $\lambda \approx 1$. For nearly equivalent Ri_0, larger ϕ increased θ, indicating a larger α_e, whereas jets with $\phi \approx 0$ had a decreased θ, indicating lower α_e.

Using our estimations for α_e and λ for the different vent shapes, ϵ and ϕ (resumed in table 2) we derived the proportion of source to local KE, noting that $(\bar{u}/\bar{u}_0)^2 \propto \lambda f(\epsilon)$ with $f(\epsilon)$ given by (5) and (6). The effect of ϵ on $(\bar{u}/\bar{u}_0)^2$ is shown in figure 6. We find that, for $\phi = 0$ from an annular vent, $(\bar{u}/\bar{u}_0)^2$ decreases with decreasing ϵ. For an annular vent with $\phi > 0$, $(\bar{u}/\bar{u}_0)^2$ increases by nearly an order of magnitude as ϵ increases from 0.09 to 0.26. Whereas we do not have enough data to establish trends for $\phi > 0$ in rectangular vents of any ϵ, for an approximately equivalent ϵ and $\phi = 0$, $(\bar{u}/\bar{u}_0)^2$ is about an order of magnitude greater for a linear vent than an annular vent.

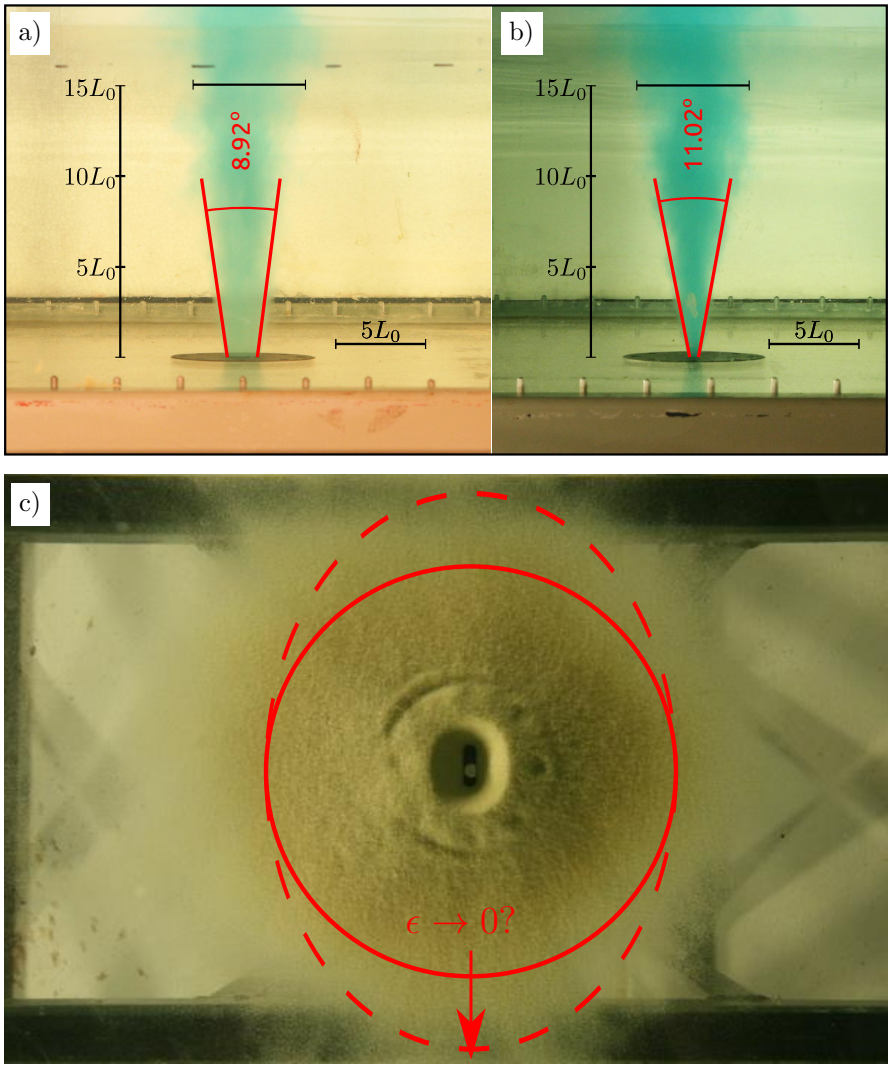

Figure 5: Experimental jet formed by a linear vent (expt. 23, $\epsilon = 0.41$) looking a) perpendicular and b) parallel to the long axis of the vent, the latter having a larger jet angle (given in degrees on both images). Scale bars, given in terms of L_0, are shown in both images and the horizontal black bars at $z = 15L_0$ are of equal length. c) Example of a deposit formed by a linear vent. We highlight the approximately circular shape of the deposit (solid line). A smaller ϵ will give more elliptical deposits (dashed lines).

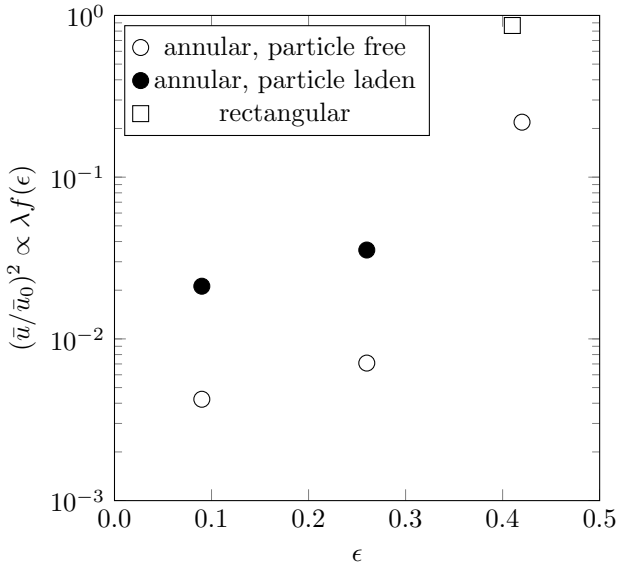

Figure 6: Prediction of KE in the jet relative to that present at the source as a function of ϵ. The functions, $f(\epsilon)$ depend on the geometry and ϵ of the vent and are given by (5)–(6).

5. Discussion and volcanological context

5.1. The distinct contributions of vent geometry and inertial particles to jet dynamics

Our results show that the entrainment coefficient, α_e, is affected by both the particle volume fraction, ϕ, and the gap size, ϵ. Entrainment is affected by gap size in two competing ways: first, small gaps generate an initial maximum eddy size that is small in comparison to the jet diameter, for example d_0 for a jet from an annular vent. Small eddies carry less angular momentum and consequently penetrate the ambient fluid to a relatively lesser extent leading, in turn, to reduced entrainment. As the largest eddies in a jet govern entrainment and their size is always constrained by the initial gap size, small gaps act to decrease α_e. This is particularly critical for high aspect ratio (i.e. elongated) vents. A second influence of the gap size on entrainment is through the shear strain rate at the source $\dot{\gamma} = u_0/l$, which is dimensionally the inverse of the eddy turnover time or the eddy rotation frequency. For narrow gaps, l is small. Thus, for a given average flow velocity, u_0, shear strain rates and eddy rotation rates are high, which enhance entrainment.

Our results also suggest that the relative balance of the competing effects of gap size on the angular momentum flux carried by eddies and on the eddy turnover time vary with vent geometry. For jets from annular vents, a small gap relative to the overall vent diameter (small ϵ) have small eddies and a reduced α_e in turn. For linear vents, by contrast, the eddy size and jet width scale with each

other. Consequently the effects of vent width on the shear strain rate exert the strongest control on entrainment and ,accordingly, α_e increases with ϵ (figures 4 and 6). For example, in our experiments where the width of the linear vent was many times smaller than its length, the shear strain rate and α_e were larger in the direction perpendicular to the long axis (i.e. $l = l_w$), hence the larger jet spreading angles seen in figure 5.

We observe that geometric anisotropy in entrainment into jets imparted near the source of linear vents does not persist very high up the jet: the turbulent spreading of internal velocity gradients causes the jet to become axisymmetric by the time it rises $\approx 15L_0$ (figure 5) consistent with Glaze et al. (2011). This mixing property of the flow can explain the approximately circular deposits for $\epsilon = 0.41$ (figure 5c). However, the vertical extent over which this anisotropy in entrainment will persist is expected to increase as ϵ becomes small (and hence the magnitude of anisotropy becomes large). Thus, we expect deposits to be increasingly elliptical in shape as $\epsilon \to 0$.

Because, compared to jets from circular vents, jets from linear vents have a large perimeter compared to their cross-sectional area Glaze et al. (2011) argued that jets from linear vents entrain a greater volume of fluid for a given mean plume speed. However, our experiments suggest that for similar conditions of ϕ_0, Ri_0 and approximately equal L_0 to the experiments of JJ14 (see curves for $\epsilon = 1$ in Fig. 4a), α_e is lower for linear vents. Furthermore, recent work on purely linear jets and plumes (i.e. $\epsilon \to 0$) has shown, assuming Gaussian profiles for velocity and buoyancy, that (Paillat and Kaminski, 2014a,b)

$$\alpha_{e,\mathrm{linear}} = \sqrt{\frac{1+\zeta^2}{2}}\mathrm{Ri}\left(1 - \left(\frac{2}{3}(1+\zeta^2)\right)^{-1/2}\right) + \frac{\sqrt{6}I_4}{2}, \tag{10}$$

$$I_4 = \int_{-\infty}^{\infty} \frac{\partial f(x^*,z)}{\partial x^*} j(x^*,z)dx^*, \tag{11}$$

where ζ is the ratio of the widths of the buoyancy and velocity profiles, I_4 is a dimensionless integral shape function involving the dimensionless velocity profile, $f(x^*,z)$, and turbulent shear stress profile, $j(x^*,z)$. A similar expression has been derived for round jets (Kaminski et al., 2005) where

$$\alpha_{e,\mathrm{round}} = \mathrm{Ri}\left(1 - \left(\frac{2}{3}(1+\zeta^2)\right)^{-1}\right) + \frac{C}{2} \tag{12}$$

where C is a combination of shape factors (similar to I_4) whose value has been shown to be about

0.135 (Kaminski et al., 2005; Carazzo and Jellinek, 2012). Assuming that $\sqrt{6}I_4 = C$, comparing (10) and (12) shows that $\alpha_{e,\mathrm{linear}} \leq \alpha_{e,\mathrm{round}}$ for equal Ri independent of ζ. Hence we conclude that linear vents have a lower entrainment efficiency than circular vents. When $\phi \approx 0$, our results for a linear vent with $\epsilon = 0.41$ ($\alpha_{e,\mathrm{linear}} \approx 0.075$) and an annular vent with $\epsilon = 0.42$ ($\alpha_{e,\mathrm{round}} \approx 0.125$) agree with these calculations.

The presence of particles resulted in α_e increasing by 25–35% for all vent geometries we tested. An increase of α_e with ϕ was also observed by JJ14 for $\epsilon = 1$ vents with of a large diameter (see also figure 4a) giving $\alpha_e = 0.16$ compared to $\alpha_e = 0.15$ for particle-free jets. JJ14 deduced that the increased α_e is related to the additional angular momentum imparted by particles bound to eddies, which cause them to overshoot more deeply into, deform and engulf the ambient fluid. Additionally, the vent exit geometry (straight/flared, narrow/broad) focuses the particle momentum flux, causing eddy stretching: when the vent is narrow and straight, the particle flux acts to vertically stretch eddies thus reducing their penetration into the ambient fluid. Adding particles to jets from $\epsilon = 1$ vents with narrow diameter therefore decreased α_e from 0.15 to 0.09 despite the increased angular momentum from the particles. Decreasing ϵ leads to small eddies so we interpret the increased α_e in the relatively narrow $\epsilon = 0.09$ vents (where the gap size was approximately equal to the narrow vent diameter of the experiments reported in JJ14) as the gain in angular momentum due to presence of particles being of lesser effect than the vertical stretching of eddies.

The work required to overturn and mix the density interface between jet and ambient fluid is extracted from the KE of the jet (Linden, 1973). Our results show that more KE is expended to do the work of overturning and mixing when ϵ is small (figure 6), due to the lack of penetration of small eddies into the ambient fluid. Hence small gap size produces eddies that are small in comparison to the overall jet diameter which thus require more KE to overturn, mix and entrain fluid into the jet.

5.2. Collapse of jets during caldera-forming eruptions

Our results can be applied to identify and understand the conditions in which catastrophic caldera-forming eruptions from spatially continuous or discontinuous ring fractures are more likely to lead to jet instability, which causes collapse and the production of pyroclastic flows. The potential for a jet of given source conditions to collapse can be determined from the conservation equations (7). We numerically integrated this system of equations using a 4th-order Runge-Kutta solver with suitable source conditions for q_0, m_0 and p_0 (figure 7). We consider particle-laden jets that are negatively buoyant at the source and that will collapse if they do not go through a buoyancy reversal. Hence

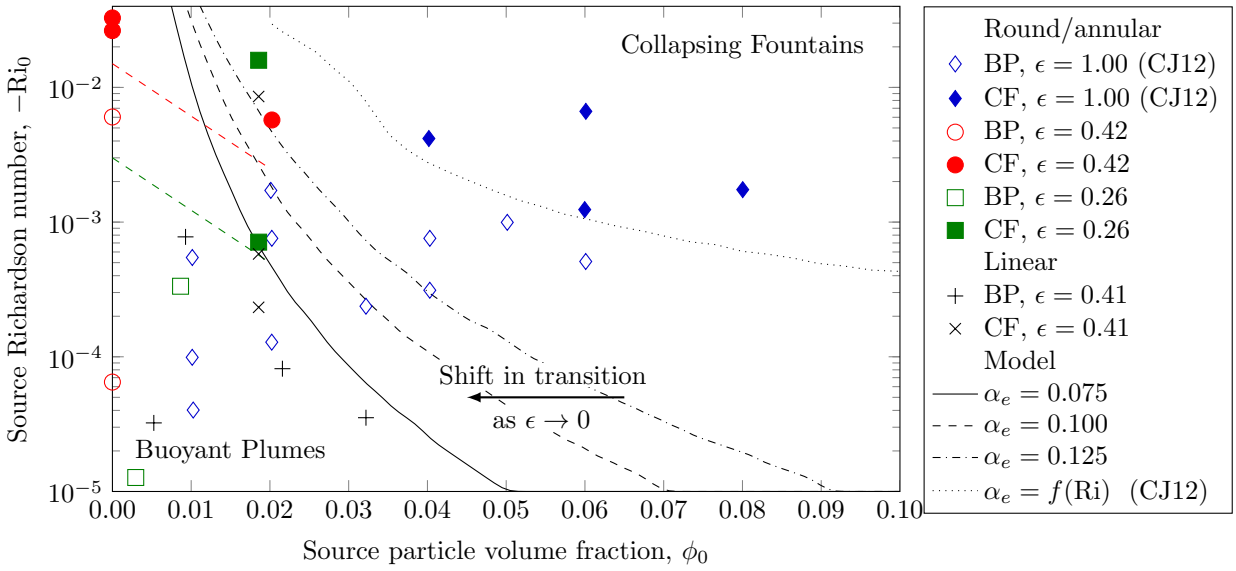

Figure 7: Regime diagram describing the theoretical transition between (stable) buoyant plumes and (unstable) collapsing fountains, given by the collapse model (7), as a function of ϕ at the source, ϕ_0, and the source Ri, $-\mathrm{Ri}_0$. The data points are the experiments from this study (cf. Table 1) and from Carazzo and Jellinek (2012) (CJ12) for a cylindrical vent (i.e. $\epsilon = 1$). The various lines give the theoretical transition from buoyant plumes to collapsing fountains using a top-hat model with different (constant) values of α_e as suggested from our experiments, and the variable entrainment model of CJ12. The arrow shows how they shift to the left as ϵ decreases. Coloured dashed lines show the approximate transitions shown by the data. In the legend text, BP = buoyant plume, CF = collapsing fountain.

if, for given initial conditions, g' remains negative at all altitudes then we determine that the jet will collapse.

Figure 7 shows a Ri_0–ϕ_0 regime diagram for the formation of buoyant plumes/collapsing fountain from circular, annular and linear vents. We include our experiments that formed a buoyant plume (BP) or a collapsing fountain (CF) (table 1) as well as those reported in Carazzo and Jellinek (2012) which are for a round jet with $\epsilon = 1$. We calculate the theoretical transition from buoyant plumes to collapsing fountains for the present model as per Carazzo and Jellinek (2012) and show these as curves, though we use a constant values of α_e as determined from our experimental data (table 2). We also give the theoretical transition using a variable entrainment coefficient as was reported in Carazzo and Jellinek (2012). It is immediately apparent from the experimental data that collapse is more likely when ϕ_0 and/or Ri_0 are large but our experiments also indicate that collapses occur in annular and linear vents at lower values of ϕ_0 and Ri_0 than in circular vents. The theoretical transition is strongly dependent on the value of α_e, and the transition curves shift towards lower ϕ_0 and Ri_0 as α_e decreases, a trend which is also seen in the experimental data as ϵ decreases (equivalent in itself to decreasing α_e). This finding supports our observation that α_e decreases with decreasing ϵ for annular vents (figure 4a). The theoretical transitions come close to capturing the actual transition when the particle fraction

is greater than about 0.02, but perform more poorly when the particle fraction approaches zero. As table 2 shows, α_e is lower for particle-free flows so that we expect a transition from larger α_e at large ϕ_0 to lower α_e at low ϕ_0. Hence theoretical models using a constant entrainment coefficient are poorly suited to capturing the rise and spread of particle-laden jets, particularly from non-round vents. A variable entrainment model (e.g. Carazzo and Jellinek, 2012, shown as dotted curve in figure 7) may be more successful but there is currently no data with which the integral shape factors in (10) and (12) can be constrained when jets contain particles or are produced from non-round vents.

In this context, we highlight that calderas have an overall diameter on the order of several kilometres or tens of kilometres for a gap length (i.e. the ring faults) on the order of a hundred metres (Lipman, 1984) so that $\epsilon_{\text{caldera}}$ is of the order of 0.1 or less. The shift in transition curves as ϵ decreases shows that collapse occurs for lower ϕ_0 and Ri. Hence we conclude that, for equal source conditions, volcanic jets produced by annular ring fractures during caldera forming eruptions are more prone to collapse and the emplacement of very-large scale ignimbrite deposits than jets from circular vents.

Our experiments involved symmetric annular vents. In nature, however, during subsidence of piston-style calderas (e.g. Lipman, 1997), feedback between the sinking block and magma has been shown to cause the block to tilt and shift laterally leading to azimuthal variation in the gap width (Folch et al., 2001; Kennedy and Stix, 2007; Kennedy et al., 2008). Assuming variation in gap width of the order of what we considered in experiments on linear vents that showed anisotropic entrainment, it is possible that natural caldera eruptions may involve anisotropic entrainment because of the variation in gap size during uneven sinking. Consequently, column collapse would occur soonest and even preferentially where the vent is narrowest (hence having the locally lowest α_e), which may show up in the deposit stratigraphy. We note also that during a piston-type caldera collapse, the width of an annular vent may vary over time if collapse of the central piston is driven by steeply inclined reverse faults, which opens the gap, while marginal blocks slide along associated normal faults, which closes the gap (Roche et al., 2000). Such a pattern would lead to complex eruptive feedback effects in the eruptive dynamics, leading to alternating phases of low or high entrainment rates and hence possible successive buoyant jet phases and collapse events.

Jets from linear vents collapse at lower Ri_0 and ϕ_0 than for round or annular jets with equivalent conditions (cf. data points for $\epsilon = 0.42$, annular vent and $\epsilon = 0.41$, linear vent in Fig. 7). This reflects the comparatively low values of α_e estimated from the jet angle data. Very large MER eruptions from linear vents have relatively large width compared to their length (Costa et al., 2011), so are likely to

have ϵ similar to our experiments and so will also have similar, low α_e. Large MER jets from linear vents are therefore prone to collapse as, not only are they very dense as ϕ is large for large MER (see table A.1 of the supplementary material), but they also have relatively small entrainment coefficients and are hence less stable. This supports field observations of large volumes of ignimbrite deposits linked to linear vent areas (Korringa, 1973; Aguirre-Diaz and Labarthe-Hernandez, 2003).

5.3. Super eruptions produce a greater proportion of pyroclastic flows

As shown in figure 1, owing to the influence of ϵ on jet stability as discussed above, the relationship between V_i/V_t and M is likely not to be straightforward, particularly when the caldera diameter becomes large. To test this, we have selected 17 silicic eruptions which represent a range of M from 5.4–9.1 for which at least two components out of the outer-caldera ignimbrite, intra-caldera fill and tephra fall volumes are known. As per Mason et al. (2004) we take V_t to be the sum of the tephra fall, intra-caldera filling and outer caldera ignimbrites. Our collated data is shown in figure 1 and given in table B.2 (supplementary material). The intra-caldera fill volume by ignimbrite is hard to constrain as i) caldera floor depth of often hard to determine unless there is full-depth faulting and ii) intra-caldera fill also contains caldera collapse material (syn- or post-eruptive, e.g. Lipman, 1984; Wilson, 2008) and hence is often poorly constrained in terms of the actual volume erupted. The volume of ignimbrite produced during silicic eruptions as a proportion of the total volume correlates with the eruption magnitude, as suggested by the arrows in figure 1. Furthermore, the data suggests that the proportion of ignimbrite increases drastically (slope doubles) at around $M_{\text{crit}} \approx 7.5$. Calderas that form in eruptions where $M < M_{\text{crit}}$ (e.g. Katmai 1912) have very much smaller overall dimensions and, assuming that the gap size is of the same order of magnitude than for large calderas, these correspond to large ϵ in our experiments. The largest eruptions therefore have $\epsilon \ll 1$, resulting in decreased entrainment and increased likelihood of PF formation. In determining the trends in figure 1, we have neglected the data for Pinatubo, Krakatau, and Minoan eruptions and the Ito Tuff (dashed ellipse). This was done for three reasons. First, strong winds carried much of the ash from the 1991 Pinatubo eruption away to the southwest where it deposited in the South China Sea (Paladio-Melosantos et al., 1996) making it nearly impossible to accurately estimate the amount of ash fall produced during the eruption leading to higher estimations of V_i/V_t. Second, the Minoan and Krakatau eruptions were strongly affected by water, meaning that the eruption dynamics were altered in favour of PF formation as heat energy was used in the water-steam phase change and could thus no-longer drive the vertical motion of the jet (Bond and Sparks, 1976; Self and Rampino, 1981). It is important here to note

that these two are also eruptions in near-coastal locations and as such much of the airborne ash may have been lost to sea. The total eruption volumes would therefore be underestimated. Third, no differentiation was made between ignimbrite and intra-caldera fill volumes for the Ito tuff (Aramaki, 1984).

6. Conclusions

Motivated by the enigmatic propensity of cataclysmic, caldera-forming eruptions to emplace very large amounts of ignimbrite relative to the total erupted volume, we have undertaken a study into the stability of particle-laden jets under conditions that are commonly found during the formation of calderas. The fissures and ring dykes that form during caldera collapse, and transport the gas and ash mixture to the surface, can be characterised as being either linear or annular vents. Furthermore, catastrophic caldera forming eruptions involve a significant proportion of inertial particles, that is particles with a Stokes number of the order of unity, that are critically coupled to the flow. Hence both these vent geometries and inertial particles are critical to the stability of eruption columns and ultimately determine whether an eruption predominantly produces buoyant plumes or pyroclastic flows.

We reproduced the dynamics of jets formed in explosive caldera-forming eruptions using scaled laboratory experiments where a particle-water mixture was injected into a tank of water. In particular, we varied the shape and aspect ratio of the vents through which these jets were formed in order to reproduce a range of vent types seen in nature. Our results were combined with a one-dimensional entrainment model to show that the presence of inertial particles and the aspect ratio of the vent play an important role in determining the dynamics of volcanic jets and the related entrainment of the ambient fluid or the collapse of the particle laden-mixture. Using this model, we measured entrainment through an entrainment coefficient along with another parameter that compared the amount of work required to overturn and mix the density interface forming the edge of the jet to the amount of kinetic energy available to do this mixing. More specifically, our experimental results and analysis favour three specific conclusions:

i) The kinetic energy (KE) extracted from turbulent jets to overturn the density interface compared to the amount available at the source is large when the vent aspect ratio is small. The ratio of KE extracted to KE available decreases as the aspect ratio increases.

ii) The addition of inertial particles to jets produced by straight-sided annular and linear vents

increased the entrainment coefficient because of the additional angular momentum transported by turbulent particle-laden eddies.

iii) The entrainment coefficient decreases when the aspect ratio of the vent decreases because eddies produced in jets from these vents are small compared to the diameter of the jet and therefore they penetrate less far into the ambient fluid and hence entrain less fluid.

Reduced entrainment stems from mechanical effects imparted as the jet exits low aspect ratio vents and these jets are unable to undergo a buoyancy reversal. When extended to volcanic jets, these findings support the conclusion that jets from caldera-forming eruptions are more likely to collapse and so produce pyroclastic flows. Therefore we should indeed expect to find that, by volume, ignimbrite forms a larger portion of the deposits from caldera-forming eruptions but that this relationship is not a straightforward function of eruption magnitude and, particularly, caldera size.

Acknowledgements

The authors thank J. Unger, for technical support and help with the experimental set-up. We also thank three anonymous reviewers for their constructive comments. DEJ was funded by a Région Auvergne-Vancouver (Canada) post-doctoral fellowship, and experiments reported here were financed by a grant from the INSU 2015 ALEAS programme. JG and AMJ were supported by NSERC. This work represents LMV/ClerVolc contribution 180.

References

Aguirre-Diaz, G. and Labarthe-Hernandez, G. (2003). Fissure ignimbrites: fissure-source origin for voluminous ignimbrites of the Sierra Madre Occidental and its relationship with basin and range faulting. *Geology*, 31(9):773–776.

Aramaki, S. (1984). Formation of the Aira Caldera, southern Kyushu, approximately 22,000 years ago. *J. Geophys. Res.-Solid Earth*, 89(NB10):8485–8501.

Bacon, C. R. (1983). Eruptive history of Mount Mazama and Crater Lake Caldera, Cascade Range, U.S.A. *J. Volcanol. Geoth. Res.*, 18(1–4):57–115.

Bond, A. and Sparks, R. S. J. (1976). The Minoan eruption of Santorini, Greece. *J. Geol. Soc.*, 132(1):1–16.

Branney, M. J., Kokelaar, B. P., and McConnell, B. J. (1992). The Bad Step Tuff: a lava-like rheomorphic ignimbrite in a calc-alkaline piecemeal caldera, English Lake District. *Bull. Volcanol.*, 54(3):187–199.

Brown, R. J. and Branney, M. J. (2004). Event-stratigraphy of a caldera-forming ignimbrite eruption on Tenerife: the 273 ka Poris Formation. *Bull. Volcanol.*, 66(5):392–416.

Burgisser, A., Bergantz, G. W., and Breidenthal, R. E. (2005). Addressing complexity in laboratory experiments: the scaling of dilute multiphase flows in magmatic systems. *J. Volcanol. Geotherm. Res.*, 141(3–4):245–265.

Carazzo, G. and Jellinek, A. M. (2012). A new view of the dynamics, stability and longevity of volcanic clouds. *Earth Planet. Sci. Let.*, 325:39–51.

Cas, R. A. F., Wright, H. M. N., Folkes, C. B., Lesti, C., Porreca, M., Giordano, G., and Viramonte, J. G. (2011). The flow dynamics of an extremely large volume pyroclastic flow, the 2.08-Ma Cerro Galan Ignimbrite, NW Argentina, and comparison with other flow types. *Bull. Volcanol.*, 73(10):1583–1609.

Cole, J. W., Milner, D. M., and Spinks, K. D. (2005). Calderas and caldera structures: a review. *Earth-Sci. Rev.*, 69(1–2):1–26.

Cole, J. W., Spinks, K. D., Deering, C. D., Nairn, I. A., and Leonard, G. S. (2010). Volcanic and structural evolution of the Okataina Volcanic Centre; dominantly silicic volcanism associated with the Taupo Rift, New Zealand. *J. Volcanol. Geoth. Res.*, 190(1–2, SI):123–135.

Costa, A., Gottsmann, J., Melnik, O., and Sparks, R. S. J. (2011). A stress-controlled mechanism for the intensity of very large magnitude explosive eruptions. *Earth Planet. Sci. Let.*, 310(1–2):161–166.

Crowe, C., Schwarzkopf, J., Sommerfeld, M., and Tsuji, Y. (1997). *Multiphase flows with droplets and particles*. Taylor & Francis.

Del Taglia, C., Blum, L., Gass, J., Ventikos, Y., and Poulikakos, D. (2004). Numerical and experimental investigation of an annular jet flow with large blockage. *J. Fluids Eng.*, 126(3):375–384.

Druitt, T. H. and Sparks, R. S. J. (1984). On the formation of calderas during ignimbrite eruptions. *Nature*, 310(5979):679–681.

Ferguson, C. A., McIntosh, W. C., and Miller, C. F. (2013). Silver Creek caldera: the tectonically dismembered source of the Peach Spring Tuff. *Geology*, 41(1):3–6.

Fischer, H., List, E., Koh, R., Imberger, J., and Brooks, N. (1979). *Mixing in Inland and Coastal Waters*. Academic Press.

Folch, A., Codina, R., and Marti, J. (2001). Numerical modeling of magma withdrawal during explosive caldera-forming eruptions. *J. Geophys. Res.-Solid Earth*, 106(B8):16163–16175.

Folch, A. and Martí, J. (2004). Geometrical and mechanical constraints on the formation of ring-fault calderas. *Earth Planet. Sci. Let.*, 221(1–4):215–225.

Glaze, L. S., Baloga, S. M., and Wimert, J. (2011). Explosive volcanic eruptions from linear vents on Earth, Venus, and Mars: comparisons with circular vent eruptions. *J. Geophys. Res.-Planets*, 116.

Hildreth, W. and Mahood, G. A. (1986). Ring-fracture eruption of the Bishop Tuff. *Geol. Soc. Am. Bull.*, 97(4):396–403.

Jellinek, A. M. and DePaolo, D. J. (2003). A model for the origin of large silicic magma chambers: precursors of caldera-forming eruptions. *Bull. Volcanol.*, 65(5):363–381.

Jellinek, M. (2014). Volcanic bipolar disorder explained. *Nat. Geosci.*, 7(2):84–85.

Jessop, D. E. and Jellinek, A. M. (2014). Effects of particle mixtures and nozzle geometry on entrainment into volcanic jets. *Geophys. Res. Lett.*, 41:1–6.

Kaminski, E., Tait, S., and Carazzo, G. (2005). Turbulent entrainment in jets with arbitrary buoyancy. *J. Fluid Mech.*, 526:361–376.

Kennedy, B. and Stix, J. (2007). Magmatic processes associated with caldera collapse at Ossipee ring dyke, New Hampshire. *Geol. Soc. Am. Bull.*, 119(1–2):3–17.

Kennedy, B. M., Jellinek, A. M., and Stix, J. (2008). Coupled caldera subsidence and stirring inferred from analogue models. *Nat. Geosci.*, 1(6):385–389.

Ko, N. W. M. and Chan, W. T. (1978). Similarity in initial region of annular jets - 3 configurations. *J. Fluid Mech.*, 84(4):641–656.

Korringa, M. K. (1973). Linear vent area of Soldier Meadow Tuff, an ash-flow sheet in northwestern Nevada. *Geol. Soc. Am. Bull.*, 84(12):3849–3865.

Kotsovinos, N. E. (1977). Plane turbulent buoyant jets. part 2. turbulence structure. *J. Fluid Mech.*, 81(JUN9):45–62.

Koyaguchi, T., Suzuki, Y. J., and Kozono, T. (2010). Effects of the crater on eruption column dynamics. *J. Geophys. Res.-Solid Earth*, 115.

Linden, P. F. (1973). Interaction of a vortex ring with a sharp density interface - a model for turbulent entrainment. *J. Fluid Mech.*, 60(3):467–480.

Lipman, P. W. (1984). The roots of ash flow calderas in western North America: windows into the tops of granitic batholiths. *J. Geophys. Res.-Solid Earth*, 89:8801–8841.

Lipman, P. W. (1997). Subsidence of ash-flow calderas: relation to caldera size and magma-chamber geometry. *Bull. Volcanol.*, 59(3):198–218. IAVCEI Symposium on Large Volcanic Eruptions at the 1995 IUGG Meeting, Boulder, Colorado, 1995.

Mason, B. G., Pyle, D. M., and Oppenheimer, C. (2004). The size and frequency of the largest explosive eruptions on Earth. *Bull. Volcanol.*, 66(8):735–748.

Miller, C. F. and Wark, D. A. (2008). Supervolcanoes and their explosive supereruptions. *Elements*, 4(1):11–15.

Morton, B. R., Taylor, G. I., and Turner, J. S. (1956). Turbulent gravitational convection from maintained and instantaneous sources. *P. Roy. Soc. Lond. A Mat.*, 234(1196).

Ogden, D. (2011). Fluid dynamics in explosive volcanic vents and craters. *Earth Planet. Sci. Let.*, 312(3–4):401–410.

Paillat, S. and Kaminski, E. (2014a). Entrainment in plane turbulent pure plumes. *J. Fluid Mech.*, 755.

Paillat, S. and Kaminski, E. (2014b). Second-order model of entrainment in planar turbulent jets at low reynolds number. *Phys. Fluids*, 26(4).

Paladio-Melosantos, M. L. O., Solidum, R. U., Scott, W. E., Quiambao, R. B., Umbal, J. V., Rodolfo, K. S., Tubianosa, B. S., Reyes, P. J. D., Alonso, R. A., , and Ruelo, H. B. (1996). Tephra falls of the 1991 eruptions of Mount Pinatubo. In *Fire and mud: eruptions and lahars of Mount Pinatubo, Philippines*, pages 513–535. University of Washington Press Seattle.

552 Raju, N. and Meiburg, E. (1997). Dynamics of small, spherical particles in vortical and stagnation
553 point flow fields. *Phys. Fluids*, 9(2):299–314.

554 Roche, O. and Druitt, T. H. (2001). Onset of caldera collapse during ignimbrite eruptions. *Earth*
555 *Planet. Sci. Let.*, 191(3–4):191–202.

556 Roche, O., Druitt, T. H., and Merle, O. (2000). Experimental study of caldera formation. *J. Geophys.*
557 *Res.-Solid Earth*, 105(B1):395–416.

558 Self, S. and Rampino, M. R. (1981). The 1883 eruption of Krakatau. *Nature*, 294(5843):699–704.

559 Smith, R. L. (1960). Ash flows. *Geol. Soc. Am. Bull.*, 71(6):795–&.

560 Veitch, G. and Woods, A. W. (2000). Particle recycling and oscillations of volcanic eruption columns.
561 *J. Geophys. Res.-Solid Earth*, 105(B2):2829–2842.

562 Walker, G. P. L., Self, S., and Wilson, L. (1984). Tarawera 1886, New Zealand - a basaltic Plinian
563 fissure eruption. *J. Volcanol. Geoth. Res.*, 21(1–2):61–78.

564 Willcock, M. A. W., Cas, R. A. F., Giordano, G., and Morelli, C. (2013). The eruption, pyroclastic
565 flow behaviour, and caldera in-filling processes of the extremely large volume (¿1290 km^3), intra- to
566 extra-caldera, Permian Ora (Ignimbrite) Formation, Southern Alps, Italy. *J. Volcanol. Geoth. Res.*,
567 265:102–126.

568 Wilson, C. J. N. (2008). Supereruptions and supervolcanoes: processes and products. *Elements*,
569 4(1):29–34.

570 Wilson, C. J. N. and Hildreth, W. (1997). The Bishop Tuff: new insights from eruptive stratigraphy.
571 *J. Geol.*, 105(4):407–439.

572 Wilson, L. (1976). Explosive volcanic eruptions III: Plinian eruption columns. *Geophys. J. R. Astr.*
573 *Soc.*, 45(3):543–556.

574 Wilson, L., Sparks, R. S. J., and Walker, G. P. L. (1980). Explosive volcanic eruptions - iv: the control
575 of magma properties and conduit geometry on eruption column behaviour. *Geophys. J. R. Astr.*
576 *Soc.*, 63(1):117–148.

577 Woods, A. W. (1988). The fluid dynamics and thermodynamics of eruption columns. *Bull. Volcanol.*,
578 50(3):169–193.

579 Woods, A. W. (2010). Turbulent plumes in nature. *Annual Rev. Fluid Mech.*, 42:391–412.

580 Woods, A. W. and Bursik, M. I. (1991). Particle fallout, thermal disequilibrium and volcanic plumes.

581 *Bull. Volcanol.*, 53(7):559–570.